Annals of Biomedical Engineering (© 2015)
DOI: 10.1007/s10439-015-1446-9

Deformable Surface Model for the Evaluation of Abdominal Aortic Aneurysms Treated with an Endovascular Sealing System

MARIANO E. CASCIARO,[1,2] SALMA EL-BATTI,[5,6,8] GILLES CHIRONI,[3,4,6] ALAIN SIMON,[3,4,6] ELIE MOUSSEAUX,[4,6,7] RICARDO L. ARMENTANO,[1] JEAN-MARC ALSAC,[4,5,6] and DAMIAN CRAIEM[1,2,3,4,6]

[1]Facultad de Ingeniería Ciencias Exactas y Naturales, Favaloro University, Solís 453, 1078 Ciudad Autónoma de Buenos Aires, Argentina; [2]Consejo Nacional de Investigaciones Científicas y Técnicas (CONICET), Buenos Aires, Argentina; [3]APHP, Centre de Médecine Préventive Cardiovasculaire, Hôpital Européen Georges Pompidou, Paris, France; [4]INSERM U970, Paris, France; [5]Service de Chirurgie Cardiaque et Vasculaire, Paris, France; [6]Université Paris-Descartes, Paris, France; [7]Service d'Imagerie Cardiovasculaire, Paris, France; and [8]Unité de Recherche en Développement, Imagerie et Anatomie, EA 4465, Université Paris 5, Paris, France

(Received 29 June 2015; accepted 1 September 2015)

Associate Editor Estefanía Peña oversaw the review of this article.

Abstract—Rupture of abdominal aortic aneurysms (AAA) is responsible for 1–3% of all deaths among the elderly population in developed countries. A novel endograft proposes an endovascular aneurysm sealing (EVAS) system that isolates the aneurysm wall from blood flow using a polymer-filled endobag that surrounds two balloon-expandable stents. The volume of injected polymer is determined by monitoring the endobag pressure but the final AAA expansion remains unknown. We conceived and developed a fully deformable surface model for the comparison of pre-operative sac lumen size and final endobag size (measured using a follow-up scan) with the volume of injected polymer. Computed tomography images were acquired for eight patients. Aneurysms were manually and automatically segmented twice by the same observer. The injected polymer volume resulted 9% higher than the aneurysm pre-operative lumen size ($p < 0.05$), and 11% lower than the final follow-up endobag volume ($p < 0.01$). The automated method required minimal user interaction; it was fast and used a single set of parameters for all subjects. Intra-observer and manual vs. automated variability of measured volumes were 0.35 ± 2.11 and 0.07 ± 3.04 mL, respectively. Deformable surface models were used to quantify AAA size and showed that EVAS system devices tended to expand the sac lumen size.

Keywords—Nellix device, Endograft, Geometrical deformed model, Endovascular repair, Abdominal aorta.

INTRODUCTION

Abdominal aortic aneurysms (AAA) are defined as a permanent and irreversible localized dilatation of the infrarenal aorta, usually associated with degradation and weakening of the vessel wall. AAA are mostly asymptomatic until they rupture, provoking sudden death in 65% of cases; it has become one of the main causes of cardiovascular mortality after hypertension and atherosclerosis.[20] The rupture of AAA is responsible for 1–3% of all deaths among men aged 65–85 years in developed countries.[29] Its incidence depends on several risk factors including age, male gender, tobacco smoking, hypertension and family history. Nonetheless, most AAA are called non-specific because they are seldom the direct consequence of a specific cause.[14]

The risk of AAA rupture depends on its size and consensus dictates that patients with large aneurysms should undergo surgical treatment.[7] The choice of the aneurysm repair procedure is still under discussion. While open surgical repair has proven to be effective in reducing the risk of rupture, endovascular repair is becoming a promising alternative with significant reduction in early morbidity and mortality.[22] Three of the main long-term adverse events of endovascular aneurysm repair (EVAR) devices are endoleaks, sac enlargement and graft displacement. In general, currently available endografts are bifurcated stents with proximal and distal attachment devices that provide fixation and prevent blood from flowing inside the aneurysm sac. However, novel endograft technologies that

Address correspondence to Damian Craiem, Facultad de Ingeniería Ciencias Exactas y Naturales, Favaloro University, Solís 453, 1078 Ciudad Autónoma de Buenos Aires, Argentina. Electronic mails: dcraiem@favaloro.edu.ar, damian@craiem.com.ar

Published online: 08 September 2015

minimize these complications are constantly emerging. Recently, Endologix (Irvine, Calif) presented the first multicenter report of the Nellix investigational device based on an endovascular aneurysm sealing system (EVAS).[5] This endograft is CE marked since 2013 and proposes a new strategy to isolate the aortic aneurysm wall from blood flow using a polymer-filled endobag that surrounds two balloon-expandable stents, which reach the iliac arteries.[10] Briefly, after a prefill procedure with contrast-enhanced saline solution, the amount of injected polymer is determined by monitoring the endobag pressure which reaches approximately 185–220 mmHg.[5] This innovative technique claims to be less prone to migration (thus avoiding endoleaks) and to be more versatile when dealing with short aneurysm necks and tortuous sac shapes.[17,21] Although commercial software for radiologist and surgeons is able to estimate AAA size,[15] simultaneous information about the pre-operative sizing procedure, the injected polymer volume and the actual post-operative endobag size is still not available. This work sought to investigate the relationship between the pre-operative dimensions of the aneurysm sac lumen and the actual volume of the filling polymer. To the best of our knowledge, this is the first study to simultaneously estimate and invasively assess AAA volumetric size changes before and after EVAS procedure.

Computed tomography (CT) scans are generally employed to evaluate the pre-operative and follow-up patient condition. Multiple segmentation strategies based on CT images were reported to describe the aneurysm geometry in 3D. The most popular choice within deformable models are deformable contours known as snakes[18] and deformable surfaces,[31] although many other are available, some based on graph cuts,[11] flood-fill[23] and water-shed algorithms.[3] Deformable models are known to require little human intervention to generate robust meshes against boundary irregularities, ensuring globally smooth and coherent surfaces between image slices.[25]

In this study, we conceived and developed a deformable surface model that mimics an elastic balloon that inflates inside the lumen of an aneurysm, in order to assess the 3D geometry. The method was inspired by previous reports[24,27] and modified to ensure minimum user interaction using a single set of parameters for the entire set of data. Improvements in mesh adaptation were introduced, and considerable efforts were made in order to minimize the number of parameters. Eight patients that were treated with a 3rd generation Nellix device were retrospectively analyzed, employing pre-operative and follow-up endograft implantation CT images. The pre-operative aneurysm lumen size, the amount of injected polymer and the post-operative endobag volume were measured, compared and discussed.

METHODS

Image Acquisition and Endovascular Repair Procedure

The current study was carried out using 64-slice CT contrast enhanced angiography scan images from the Cardiovascular Surgery Unit of the Hôpital Européen Georges Pompidou (France). The same scanner (Lightspeed VCT; GE Health care, Milwaukee, Wisconsin, USA) was used for pre-operative and follow-up images (within 1–3 months after surgery). Matrix size was 512×512 and axial slice distance was 1 mm (or less). Eight patients who had undergone infrarenal AAA repair with Nellix endoprothesis between November 2013 and June 2014 were included in this study. Each patient signed an approved informed consent before the surgery. The retrospective analysis of personal health data of study subjects had the authorization of the CNIL (Commission Nationale de l'Informatique et des Libertés) and was in accordance with the declaration of Helsinki.

Details of the last multicenter clinical trial of this device can be found elsewhere.[5] These endografts consist of dual balloon-expandable stents (diameter = 10 mm), surrounded by an endobag that is later filled with a polymer that occupies the aneurysm sac lumen (Fig. 1). This device is aimed at reducing potential endoleaks by excluding the aneurysm from blood flow while providing a stable anchoring that avoids graft migration. Full detail of the device and clinical procedures are described elsewhere.[10]

Geometrically Deformable Model (GDM)

The deformable model developed in this work is based on the publications of Park, Miller and Terzopoulos *et al.*[24,27,31] and was modified to reduce the number of user-selected parameters. Its main advantage is that the fitting process relies on a unique set of parameters valid for all scans. All of the algorithms were programmed in C++ (Embarcadero Technology, San Francisco, CA). GDM surface fitting can be separated into four steps:

- GDM structure and seeding point
- Internal and external force definition
- Cyclic pressure increase and relaxation
- Finalization criteria

GDM Structure and Seeding Point

The deformable surface initial shape is a closed spheroid balloon with triangular faces positioned by the user inside the lumen of the aneurysm. The amount of faces is determined by the user through the selection of the mean initial edge length, d_{thresh} (see Table 1).

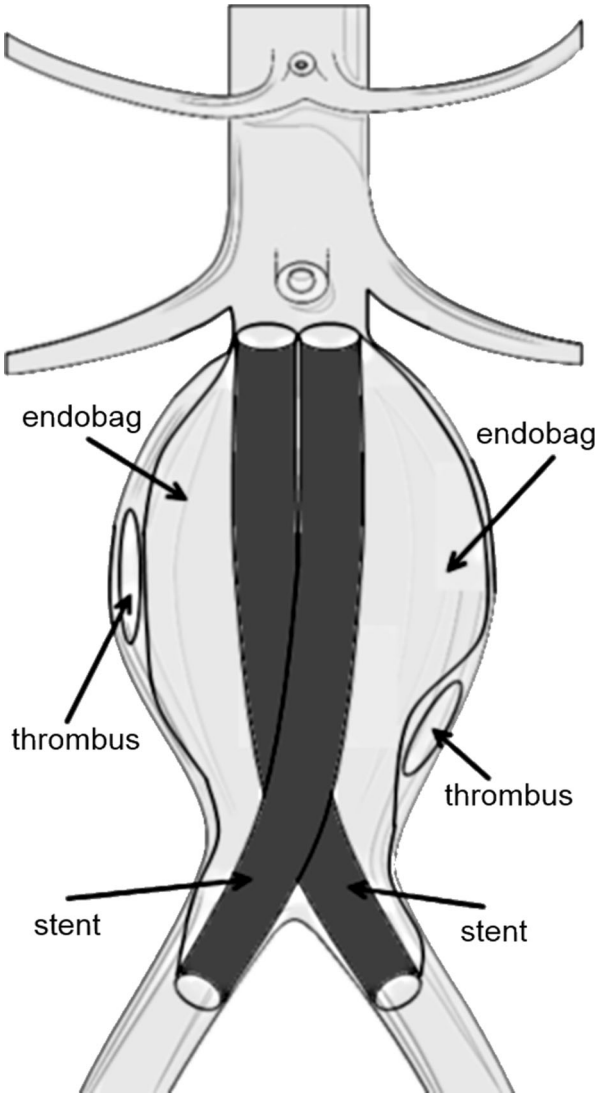

FIGURE 1. The Nellix endograft consists of two balloon-expandable stents surrounded by an endobag that is filled with polymer to stabilize the aneurysm, avoiding endoleaks.

TABLE 1. GDM parameter values.

Coefficient	Symbol	Value
Mass (milligram)	m	3.0
Damping coefficient (mN s/mm)	γ	1.5
Constant inflation force coefficient (N)	α	1.0
Minimum edge value (mm)	d_{thresh}	2.max(dX, dZ)*
Upper HU limit (HU)	$I_{\max}$	$\mu_{\max[95\%CI]} + 6 \cdot \sigma_{\max[95\%CI]}$
Lower HU limit (HU)	$I_{\min}$	$\mu_{\min[95\%CI]} - 3 \cdot \sigma_{\max[95\%CI]}$
Initial GDM radius (px)	r	20 px
Time step (iterations)	dt	1
d_{rest} re-calculation period (iterations)	T_{sizing}	20
Simulated mass injection period (iterations)	T_{adapt}	50

* dX, dZ stand for x and z spatial resolution of the TC images.

Each face consists of vertices connected by elastic edges (Fig. 2(a)). All vertices have a normal vector $\boldsymbol{n}$ that is computed from its N_F neighbor faces. "Appendix" section contains the details about mesh initialization and vertex normal vector computation.

Internal and External Force Definition

Internal forces are due to the interaction between neighboring vertices, and consist of stretching, bending and dissipative forces. The stretching force (**fs**) is the bonding strength between a vertex and its N_{v} neighbors. It is proportional to the distance between them minus the average edge length in the entire GDM, d_{rest}. Its function is to achieve a constant average distance between vertices, and is calculated as:

$$\boldsymbol{f}_s = \sum_i^{N_v} \frac{(|\Delta \boldsymbol{x}_i| - d_{rest})}{|\Delta \boldsymbol{x}_i|} \Delta \boldsymbol{x}_i, \tag{1}$$

where $\Delta \boldsymbol{x}_i$ is the vector of moduli $|\Delta \boldsymbol{x}_i|$ pointing from the vertex in the $\boldsymbol{x}$ position to its ith neighbor located at $\boldsymbol{x}_i$ (see Fig. 2(a)).

The bending force ($\boldsymbol{f}_b$) is calculated as:

$$\boldsymbol{f}_b = \Delta^C \boldsymbol{x} - \frac{1}{N_v} \sum_i^{N_v} \Delta^C \boldsymbol{x}_i, \tag{2}$$

where $\Delta^C \boldsymbol{x}$ is the average position (center of mass) of the neighbors of $\boldsymbol{x}$. The resulting $\boldsymbol{f}_b$ is a vector that points from the center of mass of $\boldsymbol{x}$ towards the averaged center of mass of all its neighboring vertices, $\Delta^C \boldsymbol{x}_i$, pushing all the centers of masses of nearby vertices towards coplanarity. Figure 2(b) shows an arbitrary configuration of a vertex, its neighbors, their centers of mass and the resulting $\boldsymbol{f}_b$.

Dissipative forces $\boldsymbol{f}_v$ are proportional to the speed of the vertex, $\boldsymbol{v}$, assuming that it is connected with non-ideal springs and/or that it is moving through a viscous fluid. The mathematical expression for this force is:

$$\boldsymbol{f}_v = -\gamma \boldsymbol{v}, \tag{3}$$

where γ is a constant damping coefficient (see Table 1).

The only external force applied to this model is an inflation force $\boldsymbol{f}^p$ that pushes each vertex of the GMD perpendicular to the surface. This force can make the mesh to locally expand or compress, morphing the GDM from a sphere into its final shape. Inflation force simulates the application of an internal pressure p_{int} on the inner surface (expansive force), and an external pressure p_{ext} exerted by the vessel walls or other structures that oppose to the advance of the GDM (compressive force). The pressure difference acting on a face j is responsible for the per-face force:

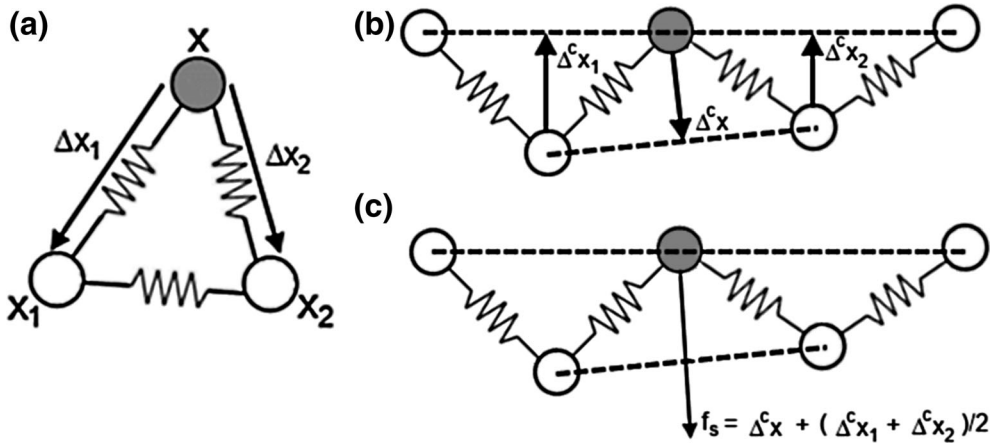

FIGURE 2. (a) GDM face representation: the vertex at position x is connected by elastic edges to its neighbor vertices x_1 and x_2. Vectors Δx_1 and Δx_2 connect x with its neighbors. (b) Shows the vector pointing from each vertex to the center of mass of its two neighbors, namely $\Delta^C x$, $\Delta^C x_1$ and $\Delta^C x_2$. (c) The resulting bending force acting on vertex x is the vector pointing towards the center of mass of its neighbors, $\Delta^C x$, minus the average of the analogous vectors from its neighbors $(\Delta^C x_1 + \Delta^C x_2)/2$.

$$\boldsymbol{f}_j^p = (p_{int} - p_{ext}) a_j \widehat{\boldsymbol{n}}_j^F = \Delta p a_j \widehat{\boldsymbol{n}}_j^F, \tag{4}$$

where a_j and $\widehat{\boldsymbol{n}}_j^F$ are the face's area and normal unitary vector, respectively. The pressure force on the GDM vertices is calculated from the force acting on the neighbor faces (details can be found in "Appendix" section). Rather than assuming a constant internal pressure over time, a non-homogeneous per-vertex pressure is defined as:

$$\Delta p = \frac{\pm\alpha}{2|\boldsymbol{n}|} \tag{5}$$

resulting in a constant per-vertex inflation force given by the expression:

$$\boldsymbol{f}^p = \pm\alpha.\widehat{\boldsymbol{n}}. \tag{6}$$

The choice of (+) or (−) signs means that the vertex is traveling through regions where $p_{\text{int}} > p_{\text{ext}}$ or $p_{\text{int}} < p_{\text{ext}}$, respectively. To define these regions, the Hounsfield Unit (HU) in position $\boldsymbol{x}$, namely HU($\boldsymbol{x}$), is evaluated. If HU($\boldsymbol{x}$) lies within the upper/lower intensity limits $I_{\min}$, $I_{\max}$, (+) sign is chosen in Eq. (6), whereas (−) sign is selected otherwise. The values for these intensity limits are calculated from the voxels contained inside the initial spheroid, as explained later in the Model Parameters section. This HU range is expected to include the aneurysm lumen, and to exclude all other tissues (vessel wall, thrombotic regions, *etc.*). Negative sign is also considered if the vertex position is outside user-defined upper and lower limits of the endografts (see Semi-automatic measurements section). The α constant parameter is the magnitude of the resulting expansion or contraction due to the inflation force.

Cyclic Pressure Increase and Relaxation

Our deformable model introduces an original cyclic inflation/relaxation process simulated by the repetition of two iterative steps:

(i) Periodic internal volume injection: it is achieved by increasing the total GDM vertices through the subdivision of all faces having at least one side larger than the mean initial edge length, d_{thresh}. These subdivision stake place every T_{adapt} iterations. The new vertices increase the total model mass and inner pressure without significantly changing GDM surface.

(ii) GDM relaxation: when the new-born vertices begin to spread by the inflation force, inner pressure falls again due to an increase in the GDM surface. This vertex expansion takes place between consecutive T_{adapt} seconds. To simulate an internal force relaxation, every T_{sizing} seconds (with $T_{\text{sizing}} < T_{\text{adapt}}$) the mean average edge distance parameter d_{rest}, is recalculated. This reduces the magnitude of the stretching force allowing the newly injected mass to undergo adaptive size restrictions (Fig. 3).

Finalization Criteria

The net pressure exerted on the GMD inner and outer surface at a given simulation time is estimated as the area-weighted average over all GDM faces:

$$p(t) = \frac{\sum f_i^p}{\sum a_i} = \alpha \frac{N_+ - N_-}{A(t)}, \tag{7}$$

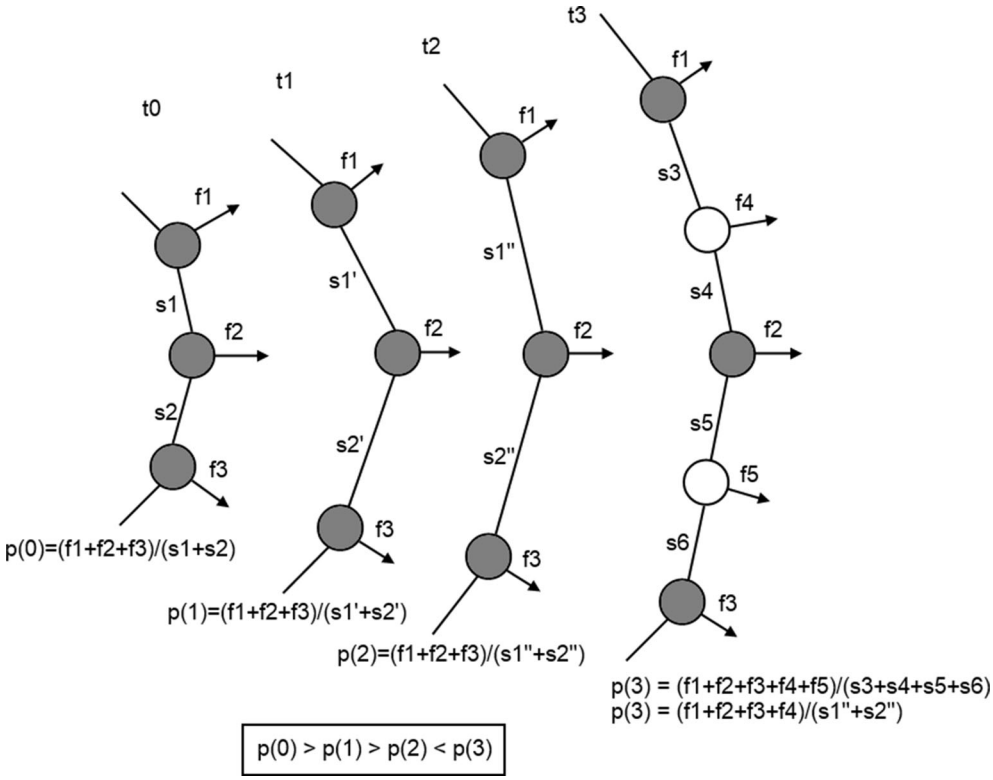

FIGURE3. From instant t_0 to t_2 the gray vertices of the GDM are spreading due to external forces (f_1 to f_3), making surface $s_1 + s_2$ increase to $s_1'' + s_2''$ and generating a pressure drop. At t_3, subdivision results in two new white vertices (and two new force terms) generating a pressure increase.

where N_+ and N_- are the amount of vertices that are in a state of expansion or compression (respectively) and $A(t)$ is the GDM surface. When $N_+ \approx N_-$ internal pressure approaches zero, thus ending the model deformation. A dimensionless pressure curve for a typical inflation sequence (normalized by the parameter α) can be found in the supplementary material.

Model Parameters

The single set of 10 model parameters employed for all patients are shown in Table 1. Seven of these parameters have constant values: mass (m), damping coefficient (γ), inflation force (α), initial sphere radius (r), time step (dt), and the two constant times that regulate the subdivision and relaxation cyclic processes (T_{sizing} and T_{adapt}). Three parameters are calculated when the user initially positions the balloon: minimum edge value (d_{thresh} calculated with the spatial resolution of the scan) and the upper/lower intensity limits (I_{max} and I_{min}) measured in Hounsfield Units. These intensity limits are calculated using mean and standard deviation of the HU values of the voxels inside the initial spheroid.

Semi-automatic Measurements

All aneurisms were segmented by the same operator. Firstly, the upper and lower limits of the endografts were determined visually in the follow-up scan. This information was then transferred to the pre-operative scan, in order to constrain the growth of the GDM. Distances fixed with respect to anatomical landmarks (e.g., renal and iliac arteries) were used for this purpose. Secondly, the user positioned a virtual balloon inside the AAA and started the inflation process. Intensities inside this initial balloon were used to compute mean and standard deviation values and to set the deformable model parameters. While the sequential expansion and subdivision steps took place, the internal pressure was monitored until it dropped below the configured threshold and the GDM finally conformed to the shape of the aneurysm. The same procedure was repeated in the follow-up scan. In this case, the balloon was positioned inside the polymer-filled endobag of the device after the stents removal. This virtual subtraction was achieved by a standard region growing algorithm, starting in a user-selected pixel belonging to the stent. All connected neighbors intensities were replaced by the mean intensity value

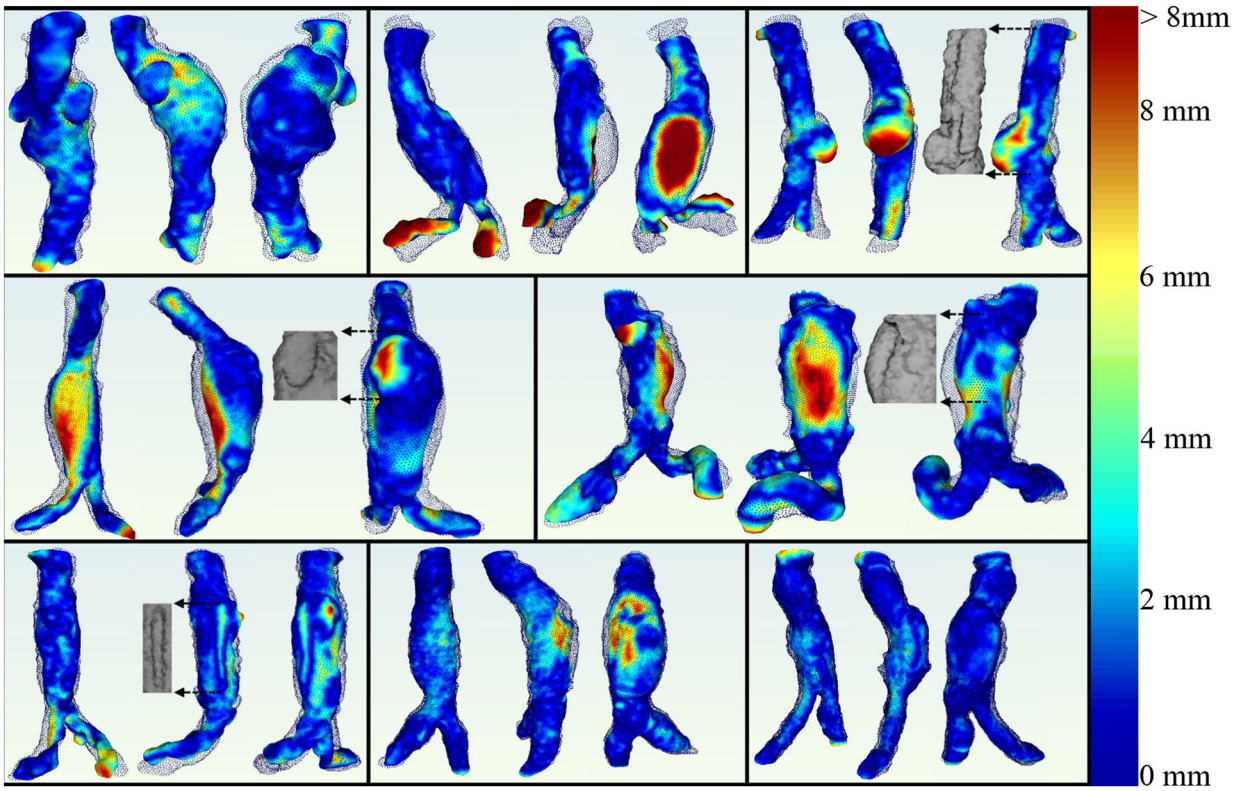

FIGURE 4. Front, side and rear views of the segmentation process in the entire dataset. Pre-operative sac lumen GDM is colored using a Haussdorff metric scale. Superimposed dots are the vertices of the follow-up endobag GDM. Black arrows point at regions of the endobag surface containing large air pockets.

inside the initial balloon. The whole automated measurement was repeated twice by the same expert after a week. Finally, the volumes and maximum axial diameter for the pre-operative sac lumen and the follow-up endobag were calculated for each patient. Pre-operative and follow-up GDMs were automatically aligned trough an Iterative Closest Points algorithm,[6] and surface distances were calculated using Haussdorff metrics.[8]

Manual Validation

A manual validation was carried out for all subjects. The contours of the pre-operative aneurysm sac lumen and of the endobag (after surgery) were manually traced by a single expert every 10 axial slices and integrated to calculate the aneurysm volume.

Statistical Analysis

Two volumes were assessed for each patient: (i) $V_{\text{pre-op}}$: pre-operative aneurysm lumen volume, (ii) $V_{\text{post-op}}$: the follow-up expanded device volume. The volume of the entire deployed device after the polymer injection (V_{deployed}) was calculated by adding the volume of injected polymer to the volume of the device endoframe containing the stents. The latter was calculated assuming an external diameter of 11 mm (10 mm stent + 1 mm polyester sleeve) and the specific stent length used for each patient. Both assessed volumes, expressed as % of change with respect to V_{deployed} were plotted individually. Pre-op and post-op maximum transverse diameters ($D_{\text{pre-op}}$ and $D_{\text{post-op}}$) were automatically calculated through the intersection of axial planes with the GDM surface. Values were expressed as mean ± standard deviation.

Semi-automatic vs. manual and intra-observer repeated measures were compared using the Bland–Altman method.[4] Accordingly, correlation coefficients, means and differences were calculated and residues were plotted.

Matched comparisons of $V_{\text{pre-op}}$ and $V_{\text{post-op}}$ with V_{deployed}, $D_{\text{pre-op}}$ with $D_{\text{post-op}}$, manual vs. automated volumes and intra-observer measurements were made using a Wilcoxon signed-rank test. A significance threshold value of $p < 0.05$ was employed.

RESULTS

All aneurysms were successfully segmented with the automated method. The user-positioned initial balloon

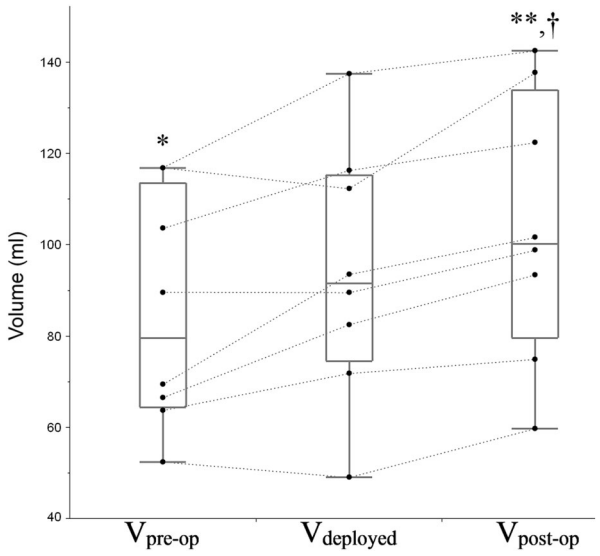

FIGURE 5. Comparison between the aneurysm lumen volume in pre-operative scan ($V_{pre\text{-}op}$), the deployed device volume that includes the injected polymer ($V_{deployed}$) and the final endobag volume during the follow-up scan ($V_{post\text{-}op}$).*$p < 0.05$ with respect to $V_{deployed}$. **$p < 0.01$ with respect to $V_{deployed}$.† $p < 0.001$ with respect to $V_{pre\text{-}op}$.

adopted its final shape in less than 10 s using a standard computer (Intel core i7, 3.4 GHz, 8 GB RAM). A slow-motion video of the GDM growing sequence in a representative patient is available as supplementary material. The length of the implanted stents was 15.8 ± 0.9 cm and the volume of injected polymer was 65.3 ± 25.4 mL.

Figure 4 shows a front, rear and side view of pre-operative and follow-up final GDM surfaces for the entire dataset colored by Haussdorff distances. Maximum and mean distances were 9.7 ± 3.6 mm (range 6.1–16.0 mm) and 1.8 ± 0.5 mm (range 1.1–2.4 mm), respectively. Higher lumen deformations (shown in red) were concentrated in the middle section of the aneurysm sac and around the iliac arteries. Note the arrows that point at visible air pockets found inside some endobags.

The measured volumes $V_{pre\text{-}op}$, $V_{deployed}$ and $V_{post\text{-}op}$ were 84.9 ± 24.5, 94.0 ± 27.8 and 103.9 ± 28.1 mL, respectively (Fig. 5). Accordingly, the deployed device volume (including the injected polymer) resulted 9% higher than $V_{pre\text{-}op}$ ($p < 0.05$), and 11% lower than

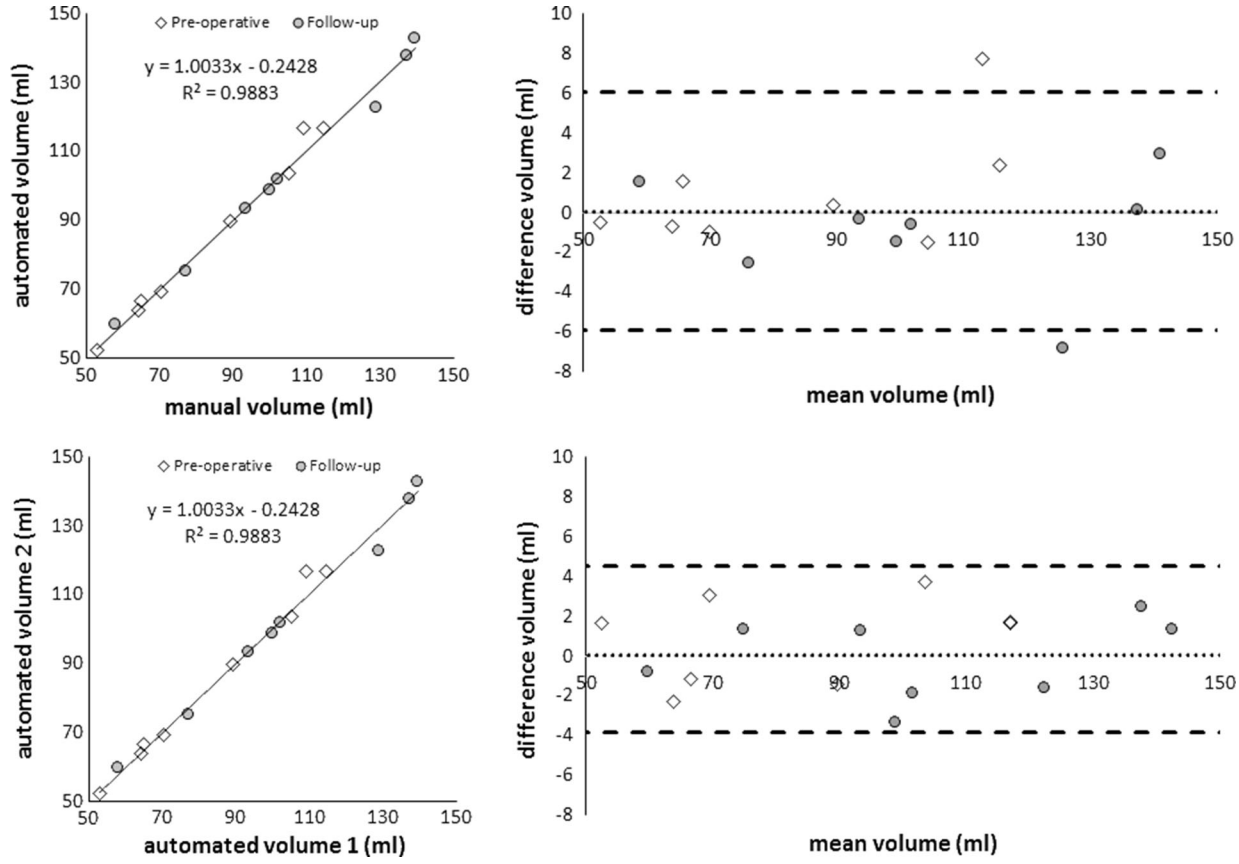

FIGURE 6. Correlations and Bland–Altman residual plots of (top) the automated vs. manual volume and (down) two different automated measurements.

$V_{post\text{-}op}$ ($p < 0.01$). In average, $V_{post\text{-}op}$ was 23% higher than $V_{pre\text{-}op}$ ($p < 0.001$). No significant differences were found between diameters $D_{pre\text{-}op}$ and $D_{post\text{-}op}$, resulting 4.36 ± 0.79 and 4.05 ± 0.57 cm, respectively.

No significant differences were found between Manual vs. Automated measurements and between two repeated measurements performed by the same observer (Fig. 6). For Manual vs. Automatic, correlation coefficient was >0.98 and mean differences were 0.07 ± 3.04 mL. Intra-observer repeatability was also high, with a correlation coefficient >0.99 and a variability of 0.35 ± 2.11 mL. In both cases, no tendencies were observed in the residual plots.

DISCUSSION

In this study, a deformable surface model was employed for the quantification of AAA lumen size before and after the implantation of a novel EVAS endograft device aimed at occupying the aneurysm sac space with a plastic endobag filled with a polymer. The proposed automated approach was fast, and it used a single set of parameters to estimate (i) the aneurysm lumen volume from a pre-operative scan and (ii) the endobag volume from a follow-up scan. We found that the amount of injected polymer was 9% higher than the aneurysm lumen sizing and 11% lower than the final endobag volume, evidencing an enlargement of the aneurysm sac after the device implantation. The use of an automated deformable surface model to reconstruct the AAA geometry helped us to analyze accurately the anatomic and technical complexity involved in the EVAR procedure, comparing virtual sizing with *in vivo* volume corroboration. All of these challenges are eventually involved in the evaluation of innovative endografts technologies as the one used in this study.

One of the major contributions of this work is the disparity found in aneurysm lumen size between pre-operative and follow-up scans with respect to the injected polymer volume. These differences should be analyzed separately. First, the amount of injected polymer was 9% higher than the estimated aneurysm size in the pre-operative scan. This might be explained by the displacement of intra-luminal thrombus during the endobag expansion. Aneurysm wall dilatation and deformation could also take place, since the polymer was injected until the endobag inner pressure reached between 185 and 220 mmHg.[5] This pressure threshold (higher than systolic arterial pressure) guaranteed the complete filling of aneurysm lumen, but systematically exceeded its size, except for two patients where 5-to-7% of the aneurysm lumen remained unoccupied (Fig. 5). Second, the size of the follow-up endobag was 11% larger than the injected polymer volume. This discrepancy is more difficult to explain, since the polymer is supposed to cure almost immediately and no long-term dilatation is expected inside the device endobag. To the best of our knowledge, polymer swellability has not been explicitly informed. Follow-up reports of change in aneurysm size have been limited to aneurysm diameter and cross sectional area but endobag volume was not reported.[21]

We speculate that some foam-like small air bubbles (not visible due to CT resolution and partial volume effect) and remains of saline solution used in the prefill procedure could remain mixed with the polymer. This could partially explain the excessive post-operative volume. Larger air pockets in the surface of the sac, not included in the GDM final volume, were visible inside seven out of eight endografts (see Fig. 4). An average of 5 air pockets (range 1–16) were found per scan, with an average total volume of 0.5 mL (range 0.1–1.5 mL). No references about these visible pockets were found in previous reports, as they may had been neglected due to their small size. Nonetheless, their presence indicates that air remains trapped inside the endobag after procedure.

Globally, if the final endobag volume is compared with the pre-operative sizing, a 23% enlargement of the sac lumen was finally forced inside the aneurysm sac. This difference was almost imperceptible in terms of maximum diameters, highlighting the necessity of volumetric measurements to describe aneurysm shapes. The degree of sac enlargement after the endograft implantation raises concern about the volume of polymer to be injected, since the aneurysm wall is generally fragile and sac expansions should be avoided in order to prevent ruptures. Although the pressure criteria seemed to be effective to almost completely fill the entire lumen, precaution should be taken about possible expansions, in the light of these results. To the best of our knowledge, this is the first study to compare a sizing procedure with its follow-up endobag volume using this EVAS endograft. Even if our measurements show that final volumes tended to be systematically higher that pre-operative sac size, these results should be analyzed with caution and need to be confirmed in a larger population.

The diagnosis of AAA is rapidly evolving by using 3D imaging techniques. *In-vivo* assessment of aneurysm sac size is thought to help predict rupture and evaluate the aneurysm progression. The surgical treatment of non-ruptured AAA is indicated based on the maximal aneurysm diameter (>5.5 cm for men and >5.0 cm for women) and its progressive growth (>1 cm/year growth).[7] This (single) diameter-based decision seems insufficient: smaller aneurysms can also rupture, whereas larger dilatations may remain intact.[33] Accordingly, we showed in this work that

although maximum diameter did not significantly change between pre-operative and follow-up measurements, volumes were significantly different. Furthermore, other approaches such as height, age and gender normalization seem clinically reasonable.[16] New imaging techniques have been contributing for decades to the better description of the aneurysms geometry and rupture prediction. Accordingly, several automated methods have been reported to assess AAA geometry.[1,9,12,19,34] To name a few, three recent examples can be found in this journal. Ayyalasomayajula *et al.*[2] reported a deformable contour model that was used to successfully segment the lumen and intra-luminal thrombus regions using 3D-snakes. Unfortunately, parameter values used to control snakes growth were not user independent, and no particular selection criteria was recommended. Shum *et al.*[30] employed a 2D algorithm based on intensity thresholding and a trained neural network to separate the inner and outer walls of AAA. They found that features such as sac length, sac height, and intra-luminal thrombus volume were more accurate than a single diameter to predict rupture. Finally, Sacks *et al.*[28] assessed the surface geometry of AAA and they found that aneurysms were highly axisymmetric, suggesting an equally complex wall tension distribution. Visibly, the main challenge of AAA segmentation aimed at predicting rupture is the separation of the lumen from thrombotic regions and the arterial wall. Modifications to include these regions into our algorithms should be envisaged in future implementations as discussed hereafter.

This study has some limitations worth mentioning. First, our segmentation method only included the aneurysm lumen and low-contrast thrombotic regions were excluded. Recent reports have revealed three distinct types of thrombus morphology with different mechanical properties.[26] A large inter-patient variation in thrombus structure, as depending on the type of thrombus present, is likely the main factor in volume discrepancies between $V_{\text{pre-op}}$ and V_{deployed}. To overcome this limitation, the modification of some parameters (e.g., the intensity limits) could be tested to include thrombotic regions and the artery wall, or thrombotic regions could be segmented separately using additional GDM. Furthermore, a Finite Element Model could be envisaged assuming the material properties for the arterial wall[32] and the thrombus.[13] Our cohort size was small, as expected from a relatively new EVAS technique. In fact, long-term follow-up data from the ongoing clinical trials is still not available, although recent reports have shown excellent procedure outcomes using this EVAS system, even with challenging aortic neck, aortic bifurcation and iliac artery anatomy.[5] Finally, even if the Nellix endograft gave us the unique opportunity to compare the pre-operative sizing with the injected polymer volume, we did not expect to find the same exact volumes in pre- and post-operative scans. Two main reasons can be mentioned: (i) the deployment of the endograft inside the aneurysm sac could actually modify the shape of the aneurysm and thrombus distribution and (ii) even if the endobag wall is extremely thin, it might fold inside the aneurysm while inflated, leaving some unfilled spaces. Rather than a sizing validation, our deformable model aimed at quantifying these volumetric differences and helping to assess the final aneurysm sac size after the device implantation. We hope this valuable information can help physicians to better anticipate issues and to reduce the risk of rupture during an endograft deployment procedure.

CONCLUSIONS

In this work, we conceived and developed a deformable surface model to compare the pre-operative sizing of AAA with respect to a polymer-filled endobag after the implantation of a novel endograft based on a sealing system (Nellix). The automated method provided fast reliable reconstructions of AAA geometry using a single set of parameters for all patients. We found that follow-up volumes were significantly larger than pre-operative sizes, indicating a possible expansion of the aneurysm sac after the endograft implantation. The use of the Nellix endograft gave us the unique opportunity to corroborate virtual sizing estimations with actual polymer volume injections. Deformable surface models seem a valuable alternative to reconstruct AAA geometry in 3D and to get insight into the evaluation of innovative endografts technologies.

ELECTRONIC SUPPLEMENTARY MATERIAL

The online version of this article (doi: 10.1007/s10439-015-1446-9) contains supplementary material, which is available to authorized users.

APPENDIX

GDM Initialization

The geometrically deformed model (GDM) starts with a regular icosahedron of unit side length. Each of its triangular faces goes through two processes: projection on a sphere of radius r, and subdivision in four new faces. This process is repeated until the average side length is less than a value d_{thresh}, chosen in order to

compromise the amount of model faces, segmentation time, and the spatial resolution of the GDM. The resulting spheroid has approximately $\frac{\pi}{\sqrt{3}}\left(\frac{r}{d_{\text{thresh}}}\right)^2$ initial faces.

Vertex Normal Computation

The vertex normal vector $\boldsymbol{n}$ is the area-weighted sum of the unitary normal vectors to all faces that share the same vertex:

$$\boldsymbol{n} = \frac{\sum_{j=1}^{N_F} a_j \widehat{\boldsymbol{n}}_j^{\boldsymbol{F}}}{\sum_{j=1}^{N_F} a_j}, \tag{A1}$$

where $\widehat{\boldsymbol{n}}_j^{\boldsymbol{F}}$ is the unitary normal vector of the j-th adjacent face, and a_j is the face area. The value of $\widehat{\boldsymbol{n}}_j^{\boldsymbol{F}}$ can be computed by cross-product:

$$\widehat{\boldsymbol{n}}_j^{\boldsymbol{F}} = \frac{\Delta \boldsymbol{x}_{1,j} \times \Delta \boldsymbol{x}_{2,j}}{\left|\left|\Delta \boldsymbol{x}_{1,j}\right| \times \left|\Delta \boldsymbol{x}_{2,j}\right|\right|} = 2\frac{\Delta \boldsymbol{x}_{1,j} \times \Delta \boldsymbol{x}_{2,j}}{a_j}, \tag{A2}$$

where $\boldsymbol{x} = (x, y, z)$ is the vertex position, and $\Delta \boldsymbol{x}_{1,j}$ and $\Delta \boldsymbol{x}_{2,j}$ are the vectors pointing from $\boldsymbol{x}$ to its two neighbor vertices in the jth adjacent face.

Inflation Force over a Vertex

The inflation force $\boldsymbol{f}^{\boldsymbol{p}}$ on a vertex is approximated by the average force over all of its N_F adjacent faces:

$$\boldsymbol{f}^{\boldsymbol{p}} = \frac{1}{N_F}\sum_{j=1}^{N_F} \boldsymbol{f}_j^{\boldsymbol{p}} = \frac{\Delta p}{N_F}\sum_{j=1}^{N_F} a_j \widehat{\boldsymbol{n}}_j^{\boldsymbol{F}} = \frac{2\Delta p}{N_F}\sum_{j=1}^{N_F} \boldsymbol{n} = 2\Delta p \boldsymbol{n}. \tag{A3}$$

Vertex Movement Simulation

Vertex movement is simulated by the kinematic equation of force-accelerated particles (Newton's second law):

$$\boldsymbol{f}(t) = m\boldsymbol{a}(t), \tag{A4}$$

where m is the mass of the vertex, $\boldsymbol{f}(t)$ is the total force acting on it and $\boldsymbol{a}(t)$ is the resulting acceleration. The term $\boldsymbol{f}(t)$ at each instant is calculated as:

$$\boldsymbol{f}(t) = \boldsymbol{f}^{\boldsymbol{p}}(t) + \boldsymbol{f}_{\boldsymbol{s}}(t) + 0.5\boldsymbol{f}_{\boldsymbol{b}}(t) + \boldsymbol{f}_{\boldsymbol{v}}(t). \tag{A5}$$

The term $\boldsymbol{f}_{\boldsymbol{v}}(t)$ requires the prior knowledge of the vertex speed $\boldsymbol{v}(t)$ at that moment, which approximated from the known values in a previous instant $t - dt$:

$$\boldsymbol{v}(t) = \boldsymbol{v}(t - dt) + \boldsymbol{a}(t - dt).dt. \tag{A6}$$

The future position of the vertex, $\boldsymbol{x}_{\boldsymbol{f}}(t)$ is calculated for the next instant $t + dt$:

$$\boldsymbol{x}_{\boldsymbol{f}}(t + dt) = \boldsymbol{x}(t) + \boldsymbol{v}(t).dt + \frac{1}{2}dt^2\boldsymbol{a}(t) \tag{A7}$$

Future position is calculated for every vertex separately, and then simultaneously updated:

$$\begin{aligned} \boldsymbol{x}(t + dt) &:= \boldsymbol{x}_{\boldsymbol{f}}(t + dt) \\ t &:= t + dt. \end{aligned} \tag{A8}$$

GDM Parameters and Selection Criteria

Mass and damping coefficient were selected after an initial calibration experiment where the spherical GDM was inflated with a constant normal force plus a random deviation of 1% of this force. After a certain time, inflation force stopped, and the mesh was allowed to relax. The quotient $m/\gamma = 2$ was found to stabilize the GDM in a number of iterations below T_{sizing} with little surface oscillation (i.e., behaving like an overdamped spring system) using a unitary time step. The HU thresholds resulted from a manual seed point selection, where the mean value and standard deviation of HU were computed inside an initial sphere of 20-pixel radius. Assuming Normal and χ^2 distribution, the 95% confidence interval was calculated for mean HU (μ) and standard deviation (σ), respectively. The upper limit was extended $+6$ times σ above the mean and the lower limit 3 times σ below the mean. This upper limit allowed the GDM to adequately expand through some bright structures (e.g., metallic stents or high concentrations of contrast agent). The lower limit was appropriate to constrain the GMD in the presence of dark structures surrounding the aneurysm lumen.

ACKNOWLEDGEMENTS

The authors thank Eng. Sandra Wray for her invaluable help in the writing of this manuscript. This work was partially supported by the project PIP Number 112-200901-00734 (CONICET).

REFERENCES

[1]Auer, M., T. C. Gasser, K. Hållfasthetslära, and T. Skolan. Reconstruction and finite element mesh generation of abdominal aortic aneurysms from computerized tomography angiography data with minimal user interactions. *IEEE Trans. Med. Imaging* 31(4):1022–1028, 2010.

[2]Ayyalasomayajula, A., A. Polk, A. Basudhar, S. Missoum, L. Nissim, and J. P. Vande Geest. Three dimensional active contours for the reconstruction of abdominal aortic aneurysms. *Ann. Biomed. Eng.* 38(1):164–176, 2010.

[3]Bieniek, A., and A. Moga. An efficient watershed algorithm based on connected components. *Pattern Recogn.* 33(6):907–916, 2000.

[4]Bland, J. M., and D. G. Altman. Statistical methods for assessing agreement between two methods of clinical measurement. *Lancet* 1(8476):307, 1986.

[5]Bockler, D., A. Holden, M. Thompson, P. Hayes, D. Krievins, J. P. de Vries, and M. M. Reijnen. Multicenter Nellix endovascular aneurysm sealing system experience in aneurysm sac sealing. *J. Vasc. Surg.* 62(2):290–298, 2015.

[6]Bouaziz, S., A. Tagliasacchi, and M. Pauly. Sparse iterative closest point. *Comput. Graph. Forum* 32(5):113–123, 2013.

[7]Buijs, R. V., T. P. Willems, R. A. Tio, H. H. Boersma, I. F. Tielliu, R. H. Slart, and C. J. Zeebregts. Current state of experimental imaging modalities for risk assessment of abdominal aortic aneurysm. *J. Vasc. Surg.* 57(3):851–859, 2013.

[8]Cignoni, P., C. Rocchini, and R. Scopigno. Metro: measuring error on simplified surfaces. *Comput. Graph. Forum* 17(2):167–174, 1998.

[9]Di Martino, E. S., G. Guadagni, A. Fumero, G. Ballerini, R. Spirito, P. Biglioli, and A. Redaelli. Fluid-structure interaction within realistic three-dimensional models of the aneurysmatic aorta as a guidance to assess the risk of rupture of the aneurysm. *Med. Eng. Phys.* 23(9):647–655, 2001.

[10]Donayre, C. E., C. K. Zarins, D. K. Krievins, A. Holden, A. Hill, C. Calderas, J. Velez, and R. A. White. Initial clinical experience with a sac-anchoring endoprosthesis for aortic aneurysm repair. *J. Vasc. Surg.* 53(3):574–582, 2011.

[11]Duquette, A. A., P.-M. Jodoin, O. Bouchot, and A. Lalande. 3D segmentation of abdominal aorta from CT-scan and MR images. *Comput. Med. Imaging Graph.* 36(4):294, 2012.

[12]Gao, L., D. G. Heath, and E. K. Fishman. Abdominal image segmentation using three-dimensional deformable models. *Invest. Radiol.* 33(6):348–355, 1998.

[13]Gasser, T. C., G. Gorgulu, M. Folkesson, and J. Swedenborg. Failure properties of intraluminal thrombus in abdominal aortic aneurysm under static and pulsating mechanical loads. *J. Vasc. Surg.* 48(1):179–188, 2008.

[14]Johnston, K. W., R. B. Rutherford, M. D. Tilson, D. M. Shah, L. Hollier, and J. C. Stanley. Suggested standards for reporting on arterial aneurysms. Subcommittee on reporting standards for arterial aneurysms, Ad Hoc Committee on Reporting Standards, Society for Vascular Surgery and North American Chapter, International Society for Cardiovascular Surgery. *J. Vasc. Surg.* 13(3):452, 1991.

[15]Kaladji, A., A. Lucas, G. Kervio, P. Haigron, and A. Cardon. Sizing for endovascular aneurysm repair: clinical evaluation of a new automated three-dimensional software. *Ann. Vasc. Surg.* 24(7):912–920, 2010.

[16]Kanaoka, Y., S. Ohgi, and T. Mori. Quantitative evaluation of abdominal aortic aneurysm. *Vasc. Endovasc. Surg.* 33(1):59–65, 1999.

[17]Karthikesalingam, A., R. J. Cobb, A. Khoury, E. C. Choke, R. D. Sayers, P. J. Holt, and M. M. Thompson. The morphological applicability of a novel endovascular aneurysm sealing (EVAS) system (Nellix) in patients with abdominal aortic aneurysms. *Eur. J. Vasc. Endovasc. Surg.* 46(4):440–445, 2013.

[18]Kass, M., A. Witkin, and D. Terzopoulos. Snakes: active contour models. *Int. J. Comput. Vision* 1(4):321–331, 1988.

[19]Kim, H. C., Y. H. Seol, S. Y. Choi, J. S. Oh, M. G. Kim, and K. Sun. A study of AAA image segmentation technique using geometric active contour model with morphological gradient edge function. *Conf. Proc. IEEE Eng. Med. Biol. Soc.* 4437–4440:2007, 2007.

[20]Kniemeyer, H. W., T. Kessler, P. U. Reber, H. B. Ris, H. Hakki, and M. K. Widmer. Treatment of ruptured abdominal aortic aneurysm, a permanent challenge or a waste of resources? Prediction of outcome using a multi-organ-dysfunction score. *Eur. J. Vasc. Endovasc. Surg.* 19(2):190–196, 2000.

[21]Krievins, D. K., A. Holden, J. Savlovskis, C. Calderas, C. E. Donayre, F. L. Moll, B. Katzen, and C. K. Zarins. EVAR using the Nellix sac-anchoring endoprosthesis: treatment of favourable and adverse anatomy. *Eur. J. Vasc. Endovasc. Surg.* 42(1):38–46, 2011.

[22]Lederle, F. A., J. A. Freischlag, T. C. Kyriakides, F. T. Padberg, Jr., J. S. Matsumura, T. R. Kohler, P. H. Lin, J. M. Jean-Claude, D. F. Cikrit, K. M. Swanson, *et al.* Outcomes following endovascular vs. open repair of abdominal aortic aneurysm: a randomized trial. *JAMA* 302:1535–1542, 2009.

[23]Lee, E. Region Filling Using Two Dimensional Grammars. *Proc. 1987 IEEE Int. Conf. Robot Autom.* pp. 147–1478, 1987.

[24]Miller, J., D. Breen, W. Lorensen, R. O'Bara, and M. Wozny. Geometrically deformed models: a method for extracting closed geometric models form volume data. *ACM* 25:217–226, 1991.

[25]Montagnat, J., H. Delingette, and N. Ayache. A review of deformable surfaces: topology, geometry and deformation. *Image Vis. Comput.* 19(14):1023–1040, 2001.

[26]O'Leary, S. A., E. G. Kavanagh, P. A. Grace, T. M. McGloughlin, and B. J. Doyle. The biaxial mechanical behaviour of abdominal aortic aneurysm intraluminal thrombus: classification of morphology and the determination of layer and region specific properties. *J. Biomech.* 47(6):1430–1437, 2014.

[27]Park, J.-Y., T. McInerney, D. Terzopoulos, and M.-H. Kim. A non-self-intersecting adaptive deformable surface for complex boundary extraction from volumetric images. *Comput. Graph.* 25(3):421–440, 2001.

[28]Sacks, M. S., D. A. Vorp, M. L. Raghavan, M. P. Federle, and M. W. Webster. In vivo three-dimensional surface geometry of abdominal aortic aneurysms. *Ann. Biomed. Eng.* 27(4):469–479, 1999.

[29]Sakalihasan, N., R. Limet, and O. D. Defawe. Abdominal aortic aneurysm. *Lancet* 365(9470):1577–1589, 2005.

[30]Shum, J., G. Martufi, E. Di Martino, C. B. Washington, J. Grisafi, S. C. Muluk, and E. A. Finol. Quantitative assessment of abdominal aortic aneurysm geometry. *Ann. Biomed. Eng.* 39(1):277–286, 2011.

[31]Terzopoulos, D., A. Witkin, and M. Kass. Constraints on deformable models: recovering 3D shape and nonrigid motion. *Artif. Intell.* 36(1):91–123, 1988.

[32]Vande Geest, J. P., M. S. Sacks, and D. A. Vorp. The effects of aneurysm on the biaxial mechanical behavior of human abdominal aorta. *J. Biomech.* 39:1324–1334, 2006.

[33]Wever, J. J., J. D. Blankensteijn, W. P. T. M. Mali, and B. C. Eikelboom. Maximal aneurysm diameter follow-up is inadequate after endovascular abdominal aortic aneurysm repair. *Eur. J. Vasc. Endovasc. Surg.* 20(2):177–182, 2000.

[34]Subasic M., Loncaric S, Fau-Sorantin E., and Sorantin E. 3-D image analysis of abdominal aortic aneurysm. (0926-9630 (Print)).